Improvements in one-dimensional grounding-line parameterizations in an ice-sheet model with lateral variations

David Pollard[1], Robert M. DeConto[2]

[1]Earth and Environmental Systems Institute, Pennsylvania State University, University Park, PA 16802, USA
5 [2]Department of Geosciences, University of Massachusetts, Amherst, MA 01003, USA

Correspondence to: David Pollard (pollard@essc.psu.edu)

Abstract. The use of a boundary-layer parameterization of buttressing and ice flux across grounding lines in a two-dimensional ice-sheet model is improved by allowing general orientations of the grounding line. This and another modification to the model's grounding-line parameterization are assessed in two settings: a narrow fjord-like domain (MISMIP+), and in future simulations
10 of West Antarctic ice retreat under RCP8.5-based climates. The new modifications are found to have significant effects on the fjord results, which are now within the envelopes of other models in the MISMIP+ intercomparison. In contrast, the modifications have little effect on West Antarctic retreat, presumably because dynamics in the wider major Antarctic basins are adequately represented by the model's previous simpler one-dimensional formulation. As future grounding lines retreat across very deep bedrock topography in the West Antarctic simulations, buttressing is weak and deviatoric stress measures exceed the
15 ice yield stress, implying that structural failure at these grounding lines would occur. We suggest that these grounding-line quantities should be examined in similar projections by other ice models, to better assess the potential for future structural failure.

1. Introduction

Analytic boundary-layer treatments of buttressing and ice velocities across grounding lines (e.g., Schoof, 2007) are usually 1-D,
20 i.e., formulated with one horizontal dimension along the flowline and no lateral variations. In ice-sheet models with two horizontal dimensions, such formulations can be used to prescribe the approximate flow across grounding lines. In our previous work (Pollard and DeConto, 2012; DeConto and Pollard, 2016), this was done simply by applying the 1-D expressions at individual one-grid-cell-wide segments separating pairs of grounded and floating cells, so that the orientation of each single-cell "grounding-line" segment is parallel to either the x or the y axis. Although this is consistent with the one-dimensional character
25 of the formulation in Schoof (2007), it neglects the actual orientation of the wider-scale grounding line, and results in non-isotropic buttressing amounts for x vs. y directions.

Here we implement a more rigorous, isotropic treatment of grounding-line buttressing and ice flow, by applying the 1-D expressions to normal flow across a more realistic grounding-line orientation that is not constrained to one or the other grid axes. In principle this is more rigorous than the previous single-cell treatment, and is expected to improve model results. We also
30 implement a modification to improve behavior with strong buttressing, and a minor improvement in crevasse depths, as described below.

Two types of experiments are used to assess the above modifications. First, simulations are performed for a fjord-like glacier confined to a relatively narrow channel, as in the MISMIP+ intercomparison (Cornford et al. 2020). Because of the confining

lateral boundaries and a central bedrock depression, grounding lines in these simulations have large two-dimensional curvatures,
35 and provide a good test for the changes implemented here. Second, much larger-scale simulations of future ice retreat in West
Antarctica are performed, forced by warming climates corresponding to the extreme RCP8.5 greenhouse gas emissions scenario.

In section 2, the modifications to the buttressing, grounding-line flux and crevasse-depth parameterizations are described in
detail. Section 3 presents results for the narrow fjord-like MISMIP+ experiments, and section 4 presents results of the West
Antarctic future simulations, comparing results for different combinations of the new model modifications. In section 5,
40 deviatoric stresses at grounding lines in West Antarctic simulations (without hydrofracturing or cliff-failure physics) are
examined, as they retreat across very deep bedrock topography in central West Antarctica in future centuries, to assess the
potential for structural failure that could lead to very rapid disintegration of the remaining ice. In an Appendix, two additional
more speculative modifications to the model's grounding-line flux parameterization are described.

2. Methods

2.1. Orientation of grounding line

45

As described in Pollard and DeConto (2012), the primary grid in the finite-difference ice-sheet model is the h-grid, with ice
thicknesses (h) defined at the center of each cell. Ice in each h-grid cell is either floating in the ocean or is grounded, depending
on the ice thickness, bedrock elevation, and sea level. At the grid-cell level, the boundary between floating and grounded-ice
regions consists of piecewise-linear segments at the edges between pairs of h-grid cells, with each edge parallel to the x or y axis
50 (Fig. 1a). The model uses an Arakawa-C grid, in which horizontal u and v velocities are staggered half a grid cell in the x and y
directions respectively, so each segment separating floating or grounded h-cells has a u or v velocity defined at its mid-point, as
indicated in Fig. 1a. (The model performs a sub-grid interpolation that refines the grounding-line position between each pair of
h-grid cells and does not coincide with the cell edge between them, but that does not affect the material presented here).
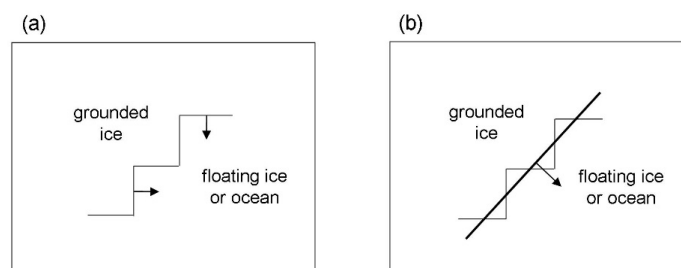
55 **Figure 1.** Schematics of grounding-line orientation treatment. Edges of h-grid cells are shown by narrow lines, with grounded ice on one side
(upper left) and floating ice or open ocean on the other (lower right). Ice velocities across grounding lines are shown by arrows. (a) Old single-
cell piecewise scheme used in earlier model versions. (b) New scheme with wider-scale grounding line orientation (thicker line) estimated by
the direction to the center-of-mass of floating ice/ocean points within a given radius.

The model ice dynamics uses a hybrid combination of vertically integrated shallow ice and shallow shelf approximations (SIA,
60 SSA), with the seaward ice flux at grounding lines imposed as a boundary condition according to an analytical expression
relating ice flux to ice thickness (Schoof, 2007):

$$q_g = \left(\frac{A(\rho_i g)^{n+1}(1-\rho_i/\rho_w)^n}{4^n C} \right)^{\frac{1}{m+1}} \theta^{\frac{n}{m+1}} \; h^{\frac{m+n+3}{m+1}} \tag{1a}$$

$$U_g = q_g \, / \, h \tag{1b}$$

where q_g is the ice flux and U_g is the ice velocity across the grounding line, and h is ice thickness at the grounding line. ρ_i and ρ_w

65   are the densities of ice and ocean water, respectively, and g is gravitational acceleration. A is the rheological coefficient and n is

the exponent for ice deformation. C is the coefficient and m is the exponent for basal sliding (Schoof, 2007), written as C_s and m_s

in Pollard and DeConto (2012). The term θ in (1a) represents buttressing by ice shelves, i.e., the amount of back stress caused by

pinning points or lateral forces on the ice shelf further downstream. The buttressing factor θ is defined as the ratio of vertically

averaged horizontal deviatoric stress normal to the grounding line, relative to its value if the ice shelf was freely floating with no

70   lateral constraints and no back stress. (The latter free-floating value is always extensional, balancing the difference between the

column-mean hydrostatic ice pressure at the grounding line with the smaller mean horizontal component of ocean-water pressure

on the ice shelf. Pinning points or lateral forces on the ice shelf reduce this value towards zero, i.e., less extensional and more

compressive, so $\theta = 1$ for unbuttressed grounding lines and diminishes towards 0 as buttressing increases.)

The analysis for grounding-line flux and buttressing in Schoof (2007) is limited to one-dimensional flowline geometry. In our

75   standard model (Pollard and DeConto, 2012), Eq.(1) is applied across individual one-grid-cell-wide segments separating pairs of

grounded and floating grid cells, so that the orientation of each single-cell "grounding-line" segment is parallel to either the x or

the y axis, as sketched in Fig. 1a. In the standard model, the buttressing factors θ_u and θ_v in the x and y directions respectively are:

$$\theta_u = \frac{4 \, \eta (\partial u/\partial x) \, h}{\rho_i (1-\rho_i/\rho_w) g h^2/2} \tag{2a}$$

$$\theta_v = \frac{4 \, \eta (\partial v/\partial y) \, h}{\rho_i (1-\rho_i/\rho_w) g h^2/2} \tag{2b}$$

80   where η is the non-linear strain-dependent ice viscosity, and the numerators in (2a,b) are 2x the deviatoric stress (times ice

thickness h) in the x or y directions.

Although this previous treatment of θ is consistent with the one-dimensional character of the formulation in Schoof (2007), it

does not capture the wider-scale orientation of the real grounding line, which does not actually run along the "staircase" single-

cell segments as in Fig. 1a. Furthermore, it results in non-isotropic θ values for the u and v staggered-grid velocities.

85   An alternative treatment of θ is described below, and sketched in Fig. 1b. The new method allows for general grounding-line

orientations running at an angle to the grid axes, and applies the ice flux given by (1) in a direction normal to this grounding line.

First, an estimate of the grounding-line orientation is needed, that represents a spatial smoothing of the boundaries of nearby

cells. A simple algorithm is used, as follows.

(i)   Consider all grid cells within a given radius R_c of the location in question (x_c, y_c), and take the average of the x and y

90   coordinates of cells with ocean or floating ice (not grounded ice), (x_o, y_o). If this radius extends beyond the domain

boundaries, virtual points are used with their grounded or floating property equal to that extended normally from the domain boundary.

(ii) Then the normal to the grounding line (in the direction towards the ocean) is $(x_o - x_c, y_o - y_c)$. The length of this vector is normalized to 1 meter, and is called (n_x, n_y) below.

95   The resulting grounding-line orientations in some MISMIP+ experiments are shown below, which show that the algorithm works as expected. The choice of radius R_c distinguishes small-scale sinuosities in the grounding line that are averaged out, and larger-scale curvilinear features that should be retained. For the relatively confined fjord MISMIP+ experiments below, R_c is set to 20 km, and for the much larger-scale Antarctic simulations it is set to 50 km. In sensitivity tests (not shown), choices of R_c between 10 to 50 km make very little difference to the results in both types of experiments.

100   This orientation is used in the calculation of N, the net deviatoric stress normal to the grounding line. The equations below follow Gudmundsson (2013, his Eqs. 2, 6 and 12).

$$N = \hat{\boldsymbol{n}}^T.(\boldsymbol{T}.\hat{\boldsymbol{n}}) \tag{3}$$

where $\boldsymbol{T}$ is the deviatoric stress tensor (Gudmundsson, 2013) and $\hat{\boldsymbol{n}}$ is the unit vector (n_x, n_y) normal to the grounding line provided by the algorithm above. Expanding in x,y coordinates, this is:

$$N = \left(2\tau_{xx} + \tau_{yy}\right)n_x{}^2 + 2\tau_{xy}n_x n_y + \left(2\tau_{yy} + \tau_{xx}\right)n_y{}^2 \tag{4}$$

where τ_{ij} are the 2D components of the stress tensor, obtained from the corresponding strain rates and viscosity η (e.g., Thoma et al., 2014):

$$\tau_{xx} = 2\eta \, \partial u/\partial x, \qquad \tau_{yy} = 2\eta \, \partial v/\partial y, \qquad \tau_{xy} = 2\eta \, (\partial u/\partial y + \partial v/\partial x)/2 \tag{5}$$

These velocities u,v are obtained from a preliminary solution of the SSA dynamical equations performed at each timestep
110   without any Schoof-imposed constraints at the grounding line (Pollard and DeConto, 2012), called the "grid-solution" below. Then the buttressing factor θ is given by

$$\theta = \frac{N}{\rho_i(1-\rho_i/\rho_w)gh/2} \tag{6}$$

The denominator is the net normal deviatoric stress that would result for a freely floating and completely unbuttressed ice shelf (or a vertical ice face with no ice shelf at all). θ is used in Eq. (1) to obtain the imposed ice flux q_g and velocity U_g normal to the
115   grounding line.

Finally, U_g (in the direction (n_x, n_y)) is resolved into its x- and y-axis components:

$$u_g = U_g \, n_x \tag{7a}$$

$$v_g = U_g \; n_y \tag{7b}$$

These velocity components are imposed in the final SSA solution at each time step, at staggered u or v-grid points as appropriate
located at the mid points between pairs of grounded and floating h-grid cells. (It is easy to show that this decomposition of U_g
onto the u and v-grids results in the physically correct net flux across the actual grounding line, averaged over many u and v-grid
points).

As well as entering in the Schoof grounding-line flux Eq. (1a), the buttressing factor θ also affects the effects of crevasses and
hydrofracturing in grounding-zone cliff-failure (Pollard et al., 2015). These physics are not enabled for all MISMIP+ runs and
most of the Antarctic runs below.

2.2. Grid-cell weighting of imposed grounding-line velocities

If the buttressing factor θ falls to zero or below in (6), this corresponds to net zero or compressive horizontal deviatoric stress
normal to the grounding line, and zero or compressive (negative) strain in the direction of flow. However, its use in the Schoof
formation for grounding-line ice velocity (1) predicts zero velocity for $\theta = 0$, and becomes invalid for $\theta < 0$, as noted by Reese et
al. (2018). In our application, θ in Eq. (1a) is restricted to be greater or equal to 0, but can still unrealistically cause the Schoof
velocity U_g to become very small or zero if θ falls to 0.

To avoid this problem, here we modify the condition (Box 9 in Pollard and DeConto, 2012) that selects the grid-cell location at
which the Schoof grounding-line velocity components u_g or v_g from (7) are imposed. First, we describe this condition in the
standard model. The following is written with all variables and indices for u velocities on the u-grid, but it applies equally to v
velocities on the v-grid.

The condition affects whether u_g is applied at the u-grid point separating a pair of floating vs. grounded h-grid cells, or at the next
downstream u-grid point. The choice depends on the difference $u_g - u_{grid}$, where u_{grid} is the "grid-solution" velocity from a
preliminary solution of the SSA equations without Schoof constrains, as mentioned above. The grounding line is assumed to be
retreating if $u_g \gg u_{grid}$, and be advancing if $u_g \ll u_{grid}$. If the former, u_g is imposed at the "actual" grounding-line location
between the pair of grounded vs. floating h-grid points, and if the latter, u_g is imposed at the next downstream (floating) location.
This rule is ad-hoc, but yields reasonable grounding-line migration in idealized tests and real-world simulations. It works
because in probable advancing situations with relatively small u_g, it is applied at the downstream edge of the first floating h-grid
cell, generally allowing it to thicken towards grounding; and in probable retreating situations with relatively large u_g, it is applied
at the downstream edge of the last grounding h-grid cell, generally allowing it to thin towards flotation.

To implement this condition, a weighting factor w (0 to 1) is used:

$$w = \max \left[\, 0, \; \min \left[\, 1, \; \left(u_g - u_{grid}\right)/U_{norm} \,\right] \,\right] \tag{8}$$

where the normalizing velocity $U_{norm} = (10^5 \text{ m}^2 \text{ yr}^{-1}) / h_g$, and h_g is the ice thickness at the grounding line. In early model versions
described in Pollard and DeConto (2012, Box 9), this was imposed as a binary choice with w either 0 or 1, i.e., as if U_{norm} in (8)

was very small. In more recent model versions the gradual weighting in (8) has been used, which was found to yield smoother

150   behavior in some tests.

The SSA equations for (u,v) over the whole domain are solved with the following impositions at the two grounding-zone points mentioned above, denoted here by u-grid indexes iau between a grounded vs. floating h-grid pair, and ibu at the next u-grid point downstream (all on the x-axis, with the y-axis index j not shown). In the standard model used to date:

At iau: $w.u_g$, $(1-w).$[*SSA equation terms at iau*]   (9a)

155   At ibu: $(1-w).u_g$, $w.$[*SSA equation terms at ibu*]   (9b)

In the SSA sparse matrix and right-hand side of the equation for u at grid point (iau, j), the first quantity of the pair in Eq. (9a) is used to weight u towards u_g with weight w, and the second quantity indicates that all other quantities (which would yield the non-Schoof "grid solution") are multiplied by $1-w$. The same is done for u at point (ibu, j), using Eq. (9b) with w and $1-w$ switched.

Here, we introduce a slight modification to the weighting, aimed at avoiding the problem of u_g becoming zero as θ falls to zero in

160   Eq. (1):

At iau: $w.u_g$, $(1-w).$[*SSA equation terms at iau*]   (10a)

At ibu: $(1-w).u_{grid}(iau)$, $w.$[*SSA equation terms at ibu*]   (10b)

The only difference from the standard model is the use in (10b) of $u_{grid}(iau)$ at point ibu instead of u_g. This term is weighted by $1-w$, so is significant in probable advancing situations with small u_g (w close to 0); the use of $u_{grid}(iau)$ at ibu still allows the first

165   floating h-grid cell to thicken sufficiently towards grounding. In the old model, as u_g falls to zero and w falls to zero, the imposed velocity at ibu in (9b) also falls to zero. In the new model, the imposed velocity in (10b) does not tend to zero, which is more reasonable. Instead, the divergence $\partial u/\partial x$ between iau and ibu tends to zero, as it should for strong buttressing causing θ to fall towards zero.

2.3. Calculation of crevasse depths

170   For all runs in this paper, an improvement is made in the parameterization of crevasse depths, used both in "normal" calving and also in the cliff-failure physics (Pollard and et al., 2015). Crevasse depths are set to the Nye-depth (at which total horizontal stress is zero for surface crevasses, or is equal to water pressure for basal crevasses; Nye, 1957; Jezek, 1984; Nick et al., 2010). Previously, the divergence $(\partial u/\partial x + \partial v/\partial y)$ was used along with ice viscosity as a simple estimate of the horizontal deviatoric stress (Pollard et al., 2015). Here, this is replaced by the maximum principal deviatoric stress (Turcotte and Schubert, 1982),

175   calculated from the strain rates and viscosity. This is a small improvement "in principle". It has no effect in the idealized fjord MISMIP+ experiments for which calving is disabled, and has little effect on the West Antarctic simulations (not shown).

3. Results: MISMIP+ experiments

As a first test of the modifications above, we use the MISMIP+ experiments (Cornford et al., 2020). These simulate glacier flow
in a rectangular fjord-like channel, and involve significant two-dimensional curvatures of grounding lines. The channel is 80 km
180   wide, with bedrock generally sloping downstream and an ice shelf flowing into the ocean. There is a bedrock depression at mid-
fjord around $x \approx 400$ km, and a ridge at $x \approx 505$ km, as shown in Fig. 2. All prescribed fields and model solutions are laterally
symmetric about the centerline of the channel. Starting from a close-to-equilibrated control state with the centerline grounding
line just downstream of the bedrock depression, prescribed perturbations to sub-ice oceanic melt rates (which are zero in the
control) are applied for 100 years, and either maintained or re-set to zero for the next 100 years. In the MISMIP+ Ice1
185   experiment, the applied oceanic melt rate is a smooth function of ice-shelf draft and ocean depth, and in the Ice2 experiment, it is
a large uniform value in the downstream section of the fjord (Cornford et al., 2020). The resulting variations of the grounding
line are examined, mainly its position along the centerline of the channel. All MISMIP+ runs here use a model resolution of 1
km, or 2 km where noted; results are very similar at these resolutions. At 5 km and coarser resolutions, the curvilinear features in
the fjord are not adequately resolved (with only 8 grid points or less in each channel half-width), and results are physically
190   unreasonable.
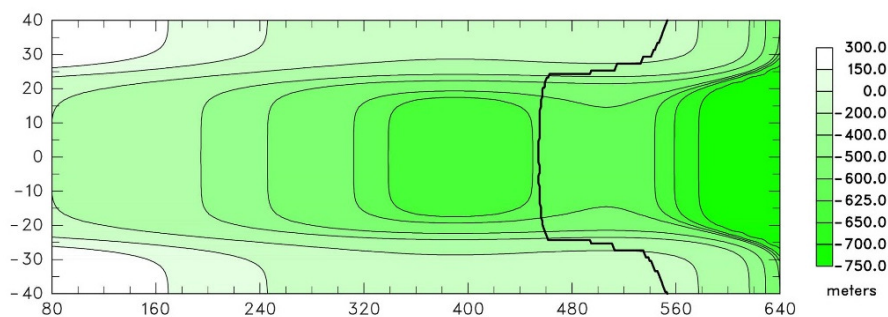
Figure 2. Bedrock topography used in the MISMIP+ experiments (Cornford et al, 2020). Also shown is the "control" grounding line after spin-up at year 0 (thick black line). Axes scales are in km. The first 80 km of the channel is not shown. Note the nearly 3x stretching of the channel width relative to the length.

195   With our standard model, i.e., without any of the modifications above, the grounding-line variations were significantly faster and
larger than other higher-order, higher-resolution models in the intercomparison (Cornford et al, 2020). Here, we perform various
sensitivity experiments with one or more of the modifications above:

   A.   the previous model with single-cell "staircase" grounding lines (Eq. 2).
   B.   the 2-D grounding-line orientation in section 2.1 (Eqs. 3 to 7).
200   C.   the 2-D orientation, and the improved grid-cell weighting in section 2.2 (Eq. 10).

Fig. 3 shows results for the MISMIP+ Ice1 experiment with the three model versions A to C. With the previous model (A,
crosses), the grounding-line variations along the centerline are close to those in our earlier experiments shown in Cornford et al.
(2020). With each new modification (B, thin lines; C, thick lines), the grounding-line variations are less rapid and have smaller
amplitude. Both modifications cause a similarly sized change. In both new experiments, the results in Fig. 3 lie within the

205   envelopes of other higher-order, higher-resolution models in the MISMIP+ intercomparison for Ice1 (shown as background shading in Fig. 3). This suggests that the modifications above are real physical improvements to our model.
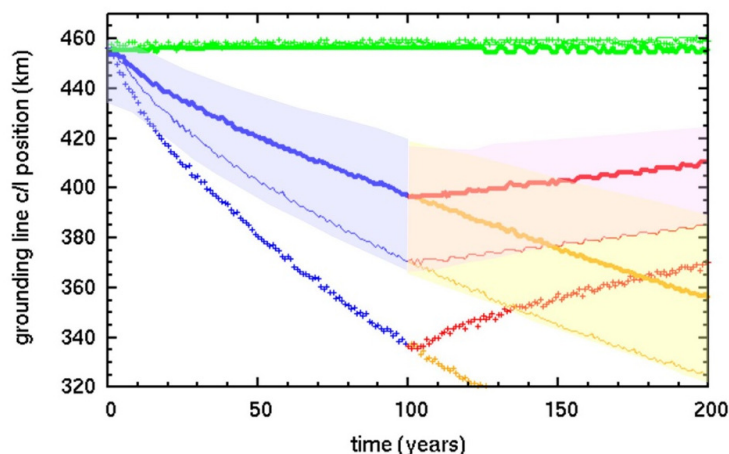
Figure 3. Along-fjord centerline position along the *x*-axis (km) of grounding lines in the MISMIP+ Ice1 experiments (Cornford et al., 2020). **Crosses:** with previous "standard" model (no modifications, version A). **Thin lines:** with new 2-D grounding-line orientation (section 2.1, version B). **Thick lines:** with new 2-D orientation and new grid-cell weighting of imposed grounding-line velocities (section 2.2, version C).
210   **Green:** control, with zero oceanic melt. **Blue and yellow:** with oceanic melt perturbation. **Red:** with oceanic melt reset to zero after year 100. Shaded regions show the envelopes for the "main subset" of MISMIP+ models, copied from Cornford et al. (2020, their Fig. 7a).

Spatial maps of ice extents, grounding lines, and buttressing factors are shown in Fig. 4, just for the model version C with both new modifications, at the beginning and end of each 100-year segment. Away from the margins, the grounding-line
215   configurations are quite similar to those for most models shown in Cornford et al. (2020); however, near the margins our grounding lines extend further downstream (to ~550 km) than most other models (~490 to 520 km). The buttressing factors in the right-hand column, not adjacent to the grounding line, are purely diagnostic and have no effect on the model physics. They are computed with Eqs. (3) to (6), but using the direction of ice flow as the normal vector instead of the grounding-line orientation algorithm (cf. Fürst et al., 2016).
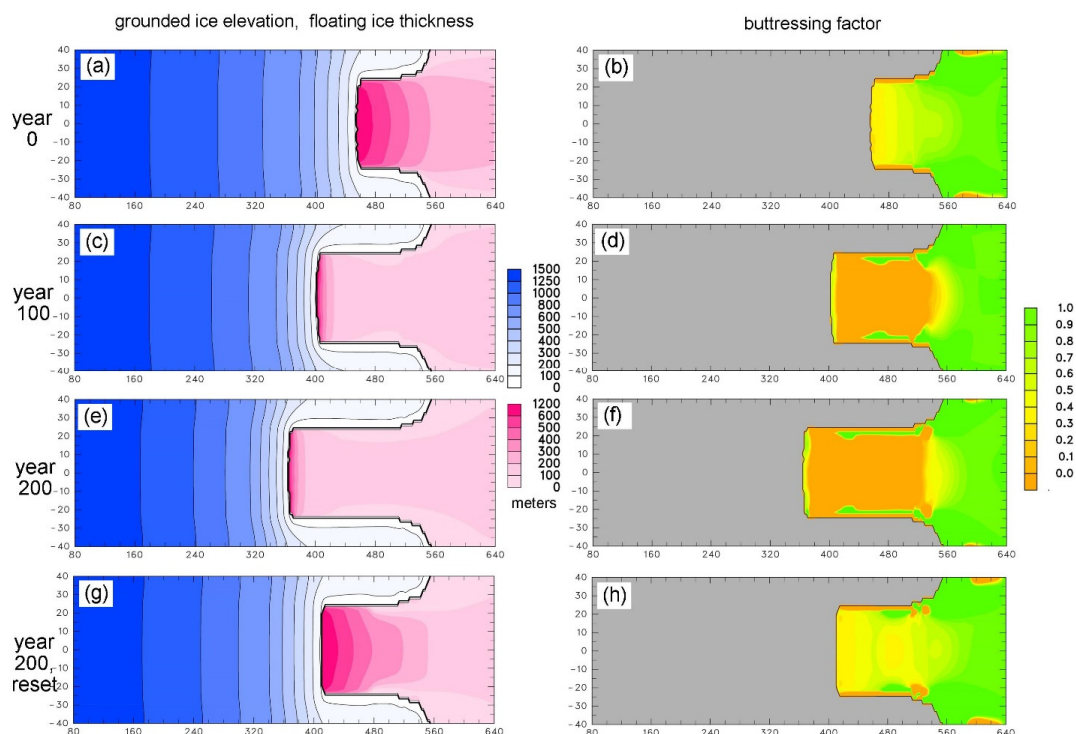
Figure 4. Spatial maps in the MISMIP+ Ice1 experiments, for model version C with both new modifications. Flow is left to right. The grounding line is shown by a thick black line. The axes scales (km), truncation of first 80 km, and stretched width are as in Fig. 2. Model resolution is 2 km for better visibility of quantities in Fig. 5. **1st row (a-b):** at year 0 (control). **2nd row (c-d):** at year 100 with oceanic melt perturbation. **3rd row (e-f):** at year 200 with oceanic melt perturbation. **4th row (g-h):** at year 200 with oceanic melt reset to zero after year 100. **1st column (a,c,e,g):** Grounded ice surface elevations (m, blue scale), and floating ice thicknesses (m, pink scale). **2nd column (b,d,f,h):** Buttressing factor θ (diagnostic except at grounding line).

Fig. 5 shows buttressing factors and grounding-line orientations, as in Fig. 4 but just at the grounding lines. The left-hand panels (buttressing factors) compare favorably with similar plots in Gudmundsson (2013, his Fig. 2). The right-hand panels (grounding-line orientations) shows that the simple algorithm described in section 2.1 works well and yields appropriate angles for these geometries.
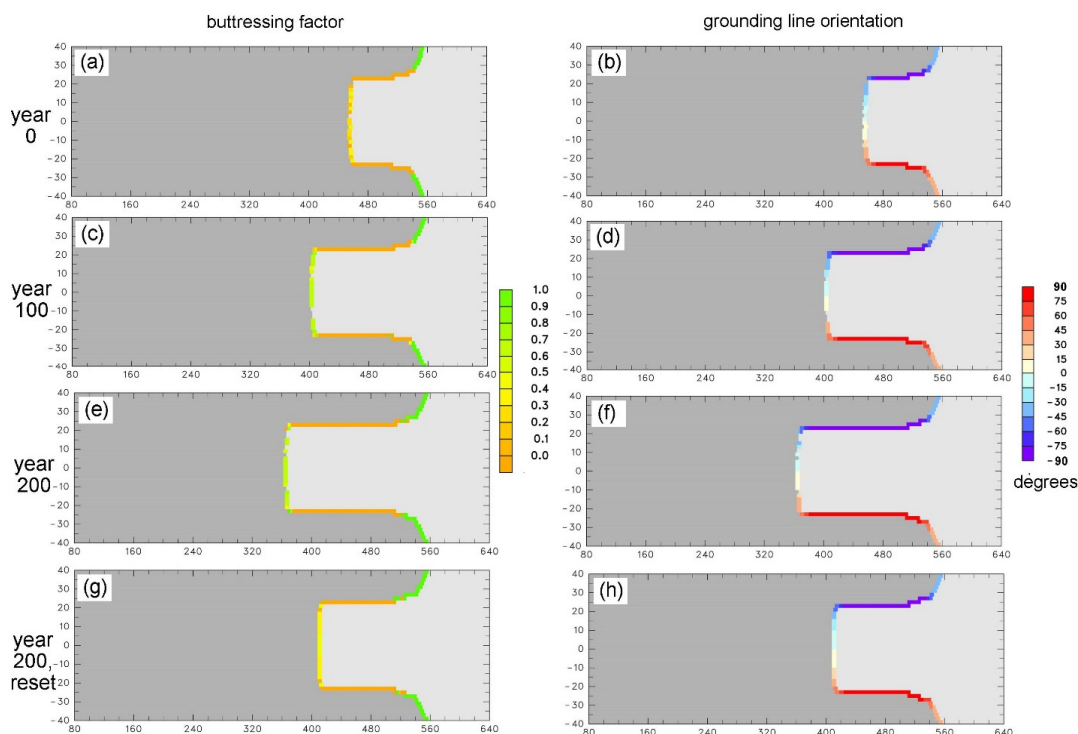
Figure 5. As Fig. 4 for quantities at grounding lines. **1st column (a,c,e,g):** Buttressing factor θ. **2nd column (b,d,f,h):** Orientation of grounding line (degrees counterclockwise of normal vector (n_x, n_y) from the along-fjord x axis, given by algorithm in section 2.1).

Centerline grounding-line variations for the Ice2 MISMIP+ experiment, with a spatially abrupt oceanic melt pattern, are shown
235   for the same three model versions in Fig. 6. The modifications have much the same effects as in Fig. 3 for the Ice1 experiment, reducing the rapidity and amplitude of the grounding-line variations compared to our previous model. As for Ice1, our new Ice2 results now lie within the envelopes of other MISMIP+ models (Cornford et al., 2020).
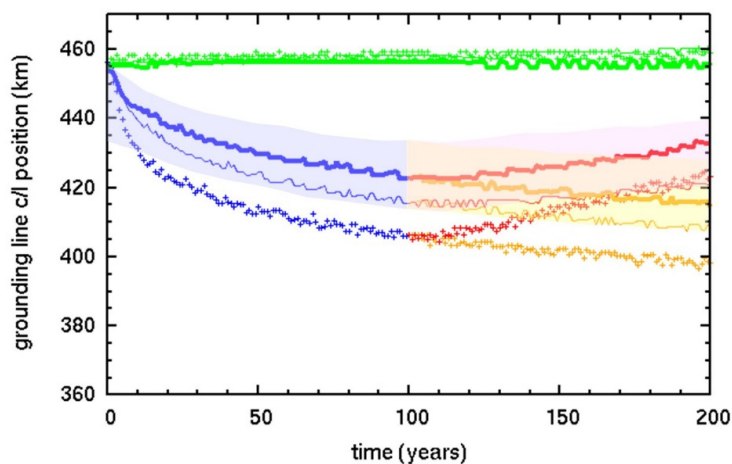
Figure 6. As Fig. 3 except for the MISMIP+ Ice2 experiments, with shading for the "main subset" of MISMIP+ models, copied from Cornford et al. (2020, their Fig. 12b).

4. Results: West Antarctic simulations

To test the modifications in real-world scenarios at larger scales than the idealized fjord experiments above, we simulate retreat of the West Antarctic ice sheet due to future climate warming. The climate forcing follows that in DeConto and Pollard (2016) for the extreme RCP8.5 greenhouse gas emissions scenario, with atmospheric temperatures and precipitation from regional climate model simulations, and oceanic temperatures from a transient future simulation with the NCAR CCSM4 global climate model (Shields et al., 2017). The ice sheet is initialized to modern observed (Fretwell et al., 2013), and run from 1950 CE for 500 years. A nested domain is used spanning West Antarctica with a polar stereographic grid of 10 km resolution, and with lateral boundary conditions supplied by an earlier continental-scale run.

The mechanisms of hydrofracturing and cliff-failure (Pollard et al., 2015; DeConto and Pollard, 2016) are disabled in the main simulations below, so the future collapse of West Antarctica is relatively slow and driven mainly by sub-ice-shelf oceanic melt and ductile processes as in other models (Feldmann and Levermann, 2015; Golledge et al., 2015; Arthern and Williams, 2017). This provides a better test of the modifications above, without the overall retreat being dominated by more drastic retreat mechanisms.

Fig. 7 shows the equivalent sea level rise corresponding to net ice melt from West Antarctica, for three types of simulations: (1) control with perpetual modern climate, (2) future RCP8.5 scenario with hydrofracturing and cliff collapse disabled, and (3) future RCP8.5 scenario with those mechanisms enabled. Each simulation is run for the same three model versions A, B and C with combinations of the new modifications, as described for the MISMIP+ experiments above.
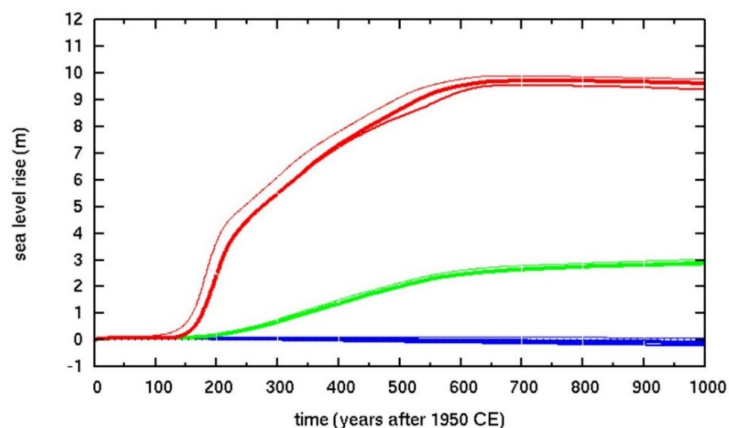
Figure 7. Equivalent global sea level rise in simulations of future West Antarctic ice retreat with climate forcing based on the RCP8.5 greenhouse gas scenario. The sea-level rise calculation accounts for ice grounded below sea level, which if melted contributes only its ice-over-flotation amount. **Thin lines:** with previous model (no modifications, version A). **Medium lines:** with new 2-D grounding-line orientation (section 2.1, version B). **Thick lines:** with new 2-D orientation and new grid-cell weighting of imposed grounding-line velocities (section 2.2, version C). **Blue:** control (perpetual modern climate). **Green:** with RCP8.5 forcing, without hydrofracturing or cliff failure. **Red:** with RCP8.5 forcing, with hydrofracturing and cliff failure.

As expected, for the future RCP8.5 simulations with no hydrofracturing or cliff failure (type 2), West Antarctic grounding lines retreat deep into the interior over several centuries. After 500 years, nearly all West Antarctic marine ice melts producing ~3 m of sea level rise, similar to that found by the other models noted above. With hydrofracturing and cliff failure enabled (type 3), much more rapid and pervasive grounding-line retreat occurs, with most West Antarctic marine ice melted within ~200 years, as in DeConto and Pollard (2016). In all simulations, the new modifications make very little difference to these results, in contrast to the MISMIP+ fjord-like experiments. Presumably this is due to the larger lateral scales and less influence of lateral boundaries in the major West Antarctic basins, so that the flow in the central regions of these basins is more 1-D (flowline) in character, better represented by the simpler "staircase" grounding-line treatment of the standard model.

Spatial maps of ice distribution and buttressing factor are shown in Figs. 8 and 9 for selected times in the future simulation without hydrofracturing or cliff failure (type 2). Except for points right at the grounding line, the buttressing factor θ in Fig. 9 is purely diagnostic and has no effect on the model physics. Away from the grounding line, θ is calculated for these figures based on stress normal to the direction of ice flow, otherwise following Eqs. (3) to (6) in section 2.1 above. There are some differences due to the new modifications (mainly for θ away from grounding lines in version A vs. B and C), but overall the distributions are similar, especially near the grounding lines where θ does enter into the model physics. For modern, the θ maps can be compared directly with those in Fürst et al. (2016), who calculated the same quantity (their K_n is our $1 - \theta$) from assimilated modern ice-shelf velocities. The patterns compare favorably for our maps with the new modifications (versions B and C).
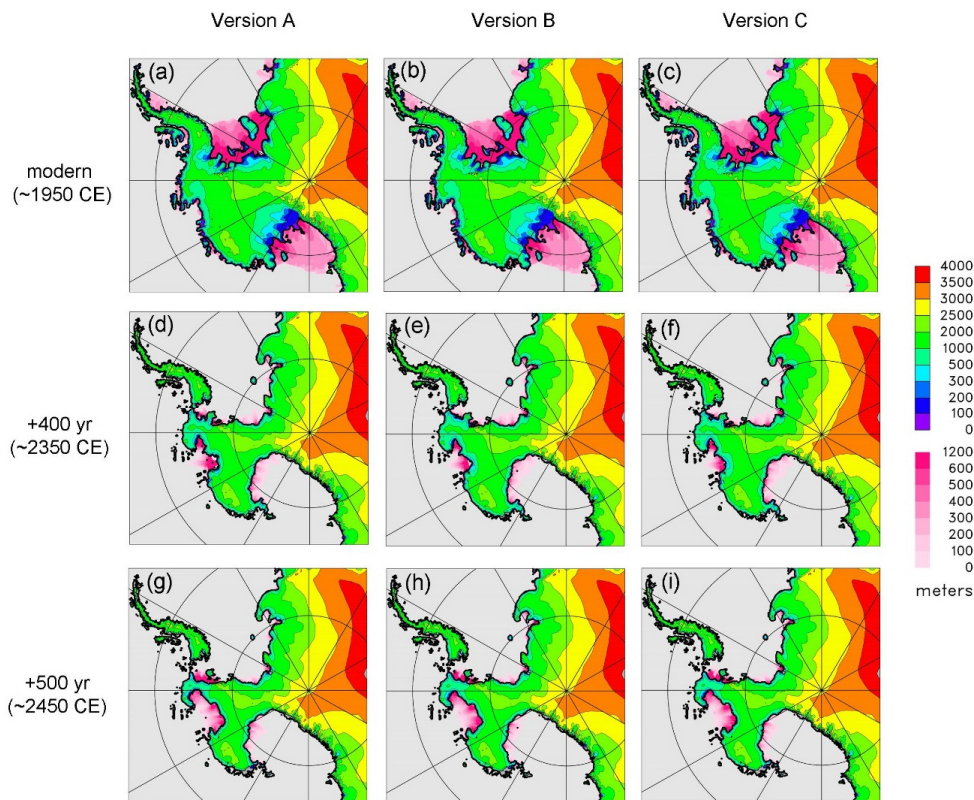
Figure 8. Spatial maps of simulated future West Antarctic ice retreat with RCP8.5 forcing, without hydrofracturing or cliff failure, showing grounded ice surface elevations (m, rainbow scale) and floating ice thicknesses (m, pink scale). **1st row (a-c):** at year 0 (~1950 CE). **2nd row (d-f):** at year 400 (~2350 CE). **3rd row (g-i):** at year 500 (~2450 CE). **1st column (a,d,g):** with earlier model version (no modifications, version A). **2nd column (b,e,h):** with new 2-D grounding-line orientation (section 2.1, version B). **3rd column (c,f,i):** with new 2-D orientation and new grid-cell weighting of imposed grounding-line velocities (section 2.2, version C).

285
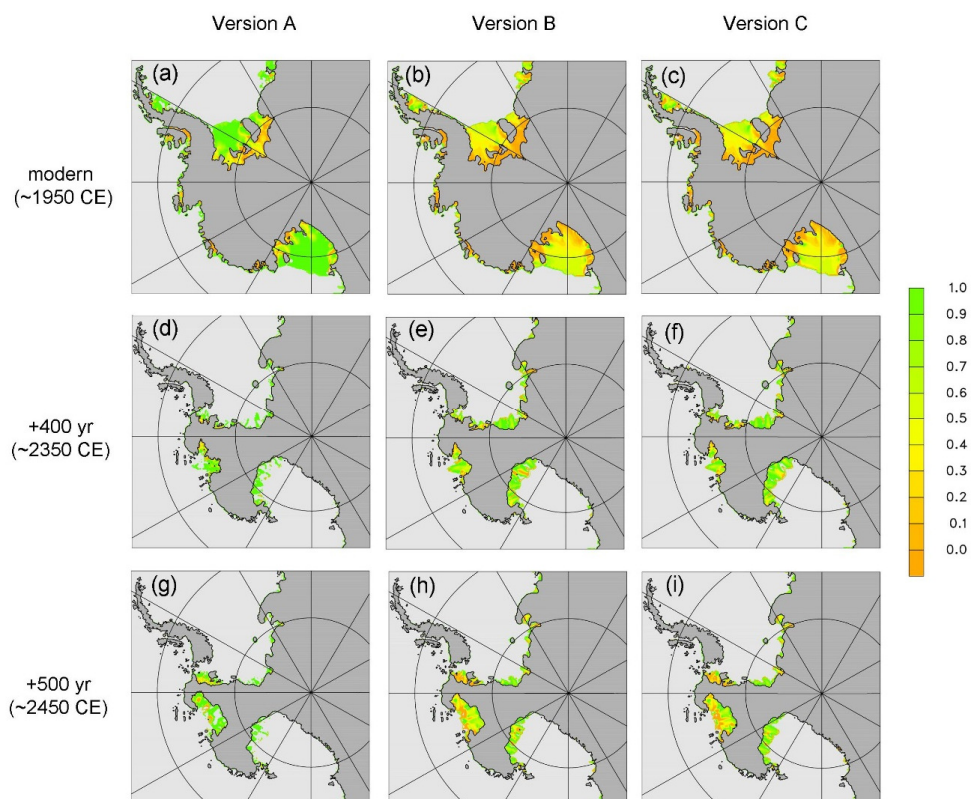
Figure 9. As Fig. 8 showing buttressing factor θ (diagnostic except at grounding line).

5. Results: potential for structural failure at West Antarctic grounding lines

290   As grounding lines retreat across central West Antarctica in the RCP8.5-driven simulations above, they encounter very deep
bathymetry with depths of ~1 to 2.5 km below sea level, especially in the Bentley Subglacial Trench (Fig. 10). Simple vertically
integrated force balance calculations (Bassis and Walker, 2012; Pollard et al., 2015) and vertically resolved modeling (Bassis and
Jacobs, 2013; Ma et al., 2017; Schlemm and Levermann, 2019; Benn et al., 2019; Parizek et al, 2019; cf. Clerc et al., 2019)
suggest that ice columns at such deep grounding lines, if unbuttressed or only weakly buttressed by ice shelves or mélange, will
295   be structurally unstable, with deviatoric stresses exceeding the material yield stress of the ice. Once initiated, structural "cliff"
failure would be expected to propagate extremely rapidly into ice upstream of the grounding line, only stopping when shallower
bathymetry is reached, or if buttressing increases somehow.
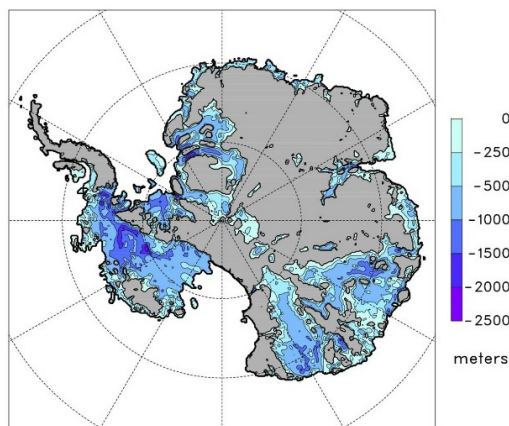
Figure 10. Modern observed Antarctic bedrock elevations where below sea level, aggregated to the 10-km model grid from Bedmap2
300 (Fretwell et al., 2013). As in Fig. 1b of Pollard et al. (2015).

In our simulations without hydrofracturing or cliff failure physics (type 2), structural failure is not part of the model, but we can use the new improved calculations of grounding-line buttressing factors and deviatoric stresses to examine the basic force balance as grounding lines traverse the deep central West Antarctic regions, and so to diagnose if structural failure would occur, or conversely, if it would be prevented by buttressing of ice shelves.

305 The relevant equation for vertical mean quantities at the grounding line, derived by simple force balance (Bassis and Walker, 2012; Pollard et al, 2015), is:

$$2\,\tau_{x'x'} = \frac{\rho_i(1-\rho_i/\rho_w)gh^2\theta}{2(h-d_s-d_b)} \qquad (11)$$

where $\tau_{x'x'}$ is the depth-averaged normal deviatoric stress at the grounding line (in direction x' to distinguish it from the model's x axis). Note that this applies equally to grounding lines with ice shelves, and to ice cliffs at grounding lines without an ice shelf
310 (for which $\theta = 1$). The crevasse depths d_s (surface) and d_b (basal) are Nye-depths as described in section 2.3 above, and depend on principal deviatoric stress. Their sum $d_s + d_s = \theta\,h\,/\,2$, where h is the ice thickness (Pollard et al., 2015).

Assuming x' is close to the horizontal principal stress direction, the quantity $2\tau_{x'x'}$ is a good approximation for the difference in the two principal stresses in the x' and z plane, which is reported in laboratory experiments as a measure of ice yield strength, typically around ~1 MPa (Bassis and Walker, 2012). Several other considerations may modify this value and the concept of a
315 uniform ice yield strength itself (Parizek et al., 2019; Clerc et al., 2019), including deformation unique to cliffs such as slumping and torques, ice cohesion and modes of failure depending on depth, and importantly, the amount of pre-existing fractures, buried crevasses, bubbly ice and/or cm-scale grain sizes, as opposed to relatively pristine ice with small (~mm-scale) grain sizes. Ice with extensive pre-existing damage is prevalent in most ice cores and presumably throughout Antarctica, and has yield strengths around ~1 MPa, much weaker than pristine ice; Parizek et al. (2019) and Clerc et al. (2019) agree that maximum heights of
320 subaerial ice cliffs (above sea level, with ~9 times that below sea level) are approximately 100 to 200 m for pre-damaged ice, and

~500 m for pristine ice. In our diagnosis below, we assume that central West Antarctic ice is typically pre-damaged (or if it is not already, it will likely become so as the rapidly retreating grounding line approaches from the north), and so assume an ice yield strength of around ~1 MPa.

325   In Fig. 11, θ and the relevant deviatoric stress measure ($2\tau_{x'x'}$ from Eq. 11) are plotted at grounding lines for the simulation without hydrofracturing or cliff failure (type 2), and for the model version C with both new modifications. For modern, $2\tau_{x'x'}$ is far below 1 MPa at all grounding lines, as it should be as no significant structural failure is observed today. At +400 years into the run (~2350 CE), when the retreating central West Antarctic grounding lines are beginning to encounter deep (>1 km) bathymetry, the surviving ice shelves shown in Fig. 8 still provide some buttressing, and most buttressing factors are well below 1; (even though these ice shelves are too short and thin to reach distant pinning points, the lateral curvature in their flow

330   produces back stress). Most $2\tau_{x'x'}$ values are somewhat below 1 MPa, indicating that extensive structural failure is unlikely.
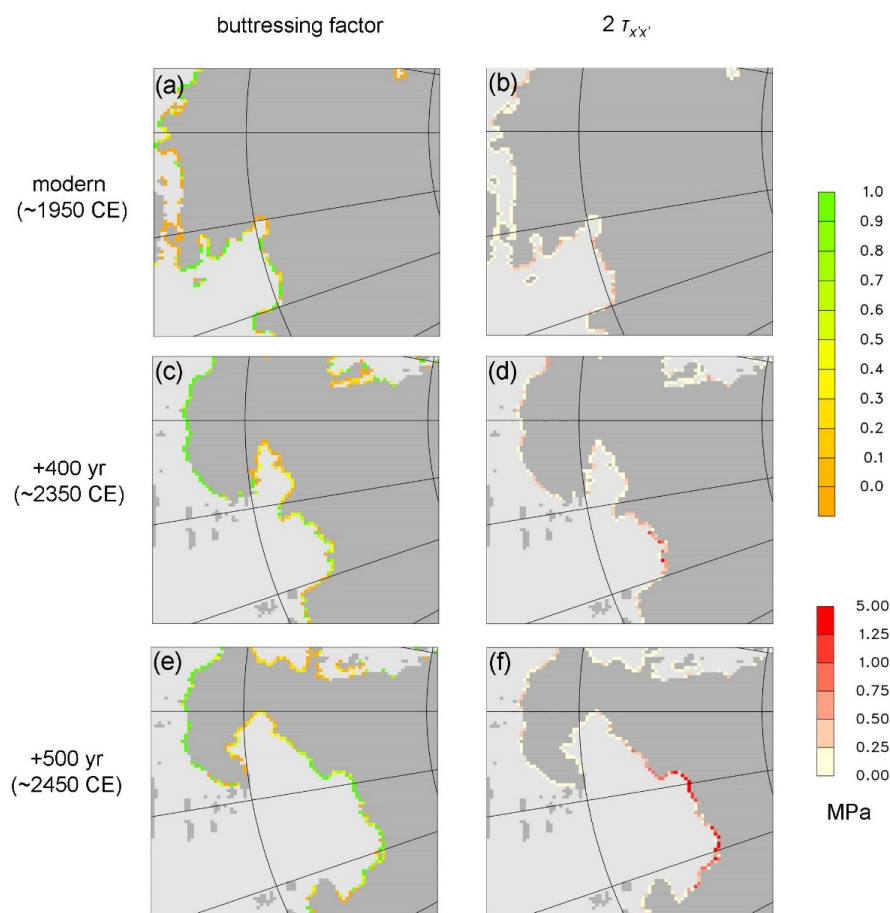
Figure 11. Grounding-line quantities in simulated future West Antarctic ice retreat with RCP8.5 forcing, without hydrofracturing or cliff failure, for model version C with both new modifications. **1st row (a-b):** at year 0 (~1950 CE). **2nd row (c-d):** at year 400 (~2350 CE). **3rd row (e-f):** at year 500 (~2450 CE). **1st column (a,c,e):** buttressing factor θ at grounding line. **2nd column (b,d,f):** $2\tau_{x'x'}$, where $\tau_{x'x'}$ is the depth-

335 averaged deviatoric normal stress at grounding lines, MPa (Eq. 11). An enlarged subset of the model domain is shown, to better show the grounding-line quantities in the central West Antarctic regions with deep bathymetry.

However, by +500 years (~2450 CE), central West Antarctic grounding lines experience even deeper bathymetry, and many θ values are at or close to 1 (weakly buttressed or essentially unbuttressed). Many $2\tau_{x'x'}$ magnitudes are at or exceed 1 MPa, indicating that structural failure of these grounding-line columns would occur.

340 **6. Discussion and Conclusions**

The modifications described and tested above in (i) 2-D orientation of the grounding line in calculating the buttressing factor and imposed normal ice flow, and (ii) grid-cell weighting of imposed grounding-line velocities, are physically reasonable. The first modification more rigorously represents the true geometry of the grounding line.

In the idealized fjord-like MISMIP+ experiments, which involve strong 2-D curvature of grounding lines in a narrow channel,
345 the modifications have significant effects on the model's grounding-line variations, bringing them in line with those of other higher-order higher-resolution models in the MISMIP+ intercomparison (Cornford et al., 2020). This suggest that the modifications are real improvements to the model physics.

In contrast, the modifications have relatively little effect in large-scale simulations of future rapid West Antarctic ice retreat. This is presumably because of the larger lateral scales of major West Antarctic basins, so that grounding-line retreat in these basins is
350 more one-dimensional in character, and better represented by the simpler "staircase" grounding-line treatment of the standard model.

The more rigorous treatments of grounding-line orientation and buttressing factors allow us to better diagnose the force balance at grounding lines in the West Antarctic simulations, to see if structural failure could occur in a future with unmitigated greenhouse-gas warming. We find that when grounding lines reach very deep central West Antarctic regions (~1 to 2.5 km below
355 sea level) after about 500 years, ice-shelf buttressing is weak and the deviatoric stress measures widely exceed the ice yield stress, implying that structural failure would occur at these grounding lines. In that case, a runaway disintegration could be initiated, with structural failure propagating very rapidly into the remaining grounded ice (Schlemm and Levermann, 2019), which in the absence of renewed buttressing would continue until shallower bathymetry is reached to the south.

Several other ice sheet-shelf models have performed similar projections of future West Antarctic retreat (e.g., Feldmann and
360 Levermann, 2015; Golledge et al., 2015; Arthern and Williams, 2017), some with higher order and/or higher resolution than ours. We suggest it would be beneficial to examine these grounding-line quantities in other model simulations, to more robustly assess the danger of structural failure in future centuries under RCP8.5-like climate warming.

Apart from ice shelves, another potential source of buttressing is from mélange. Huge amounts of floating ice debris (mélange) would be generated in front of the retreating ice fronts in the above scenarios. In major Greenland fjords today such as
365 Jakobshavn and Helheim, mélange is considered to provide significant back stress on the glacier calving front, at least in winter (e.g., Burton et al., 2018). However, in one study using a heuristic continuum model of mélange (Pollard et al., 2018), its back

stress on ice shelves and grounding lines is negligible during West Antarctic retreat. In contrast to the narrow Greenland fjords, mélange in the much wider West Antarctic embayments flows northward into the Southern oceans nearly unimpeded.

370   Other processes that could reduce the deep bathymetry encountered by future grounding lines are bedrock rebound under the reduced ice load, and less gravitational attraction of the ocean by the receding ice (Gomez et al., 2015). The West Antarctic simulations here include the first process, using a relatively simple ELRA (Elastic Lithosphere Relaxing Asthenosphere) bed model (Pollard and DeConto, 2012), and the rebound of the modern bathymetry (Fig. 10) under the central grounding lines after 400 to 500 years (Fig. 11) is minor. However, recent geophysical data indicate very low mantle viscosities below parts of West Antarctica (Heeszel et al., 2016; Barletta et al., 2018), which could produce faster rebound and shallower bathymetry by the time

375   grounding lines retreat into central regions. Work to develop Earth-sea level models with laterally varying properties and ice-ocean gravitational interaction, and couple them with ice-sheet models, is ongoing (Gomez et al., 2018; Powell et al., 2020).

Appendix

A few recent analytical studies have investigated aspects of boundary-layer treatments of grounding-line zones, going beyond Schoof (2007), such as Haseloff and Sergienko (2018) and Sergienko and Wingham (2019). Here we briefly test two

380   modifications to our grounding-line flux implementation that are more heuristic and speculative than those in the main paper. They are roughly motivated by the recent work although they cannot represent it directly and address different aspects.

A1. Strain softening

This modification addresses the presumed underestimate of strain softening in the grounding zone in a purely 1-D flowline treatment such as Schoof (2007). With no lateral variations, the second invariant of the horizontal strain tensor, entering in ice

385   viscosity in the SSA equations, is

$$\dot{\varepsilon}_{1D}^2 = (\partial u/\partial x)^2 \tag{A1}$$

as in Schoof (2007). With lateral variations and two-dimensional flow, it is

$$\dot{\varepsilon}_{2D}^2 = (\partial u/\partial x)^2 + (\partial v/\partial y)^2 + (\partial u/\partial x)(\partial v/\partial y) + \frac{1}{4}(\partial u/\partial y + \partial v/\partial x)^2 \tag{A2}$$

Then the ice viscosity η is

390   $$\eta = \frac{1}{2\,A^{1/n}\,\dot{\varepsilon}^{(n-1)/n}} \tag{A3}$$

(e.g., Thoma et al., 2014), where $\dot{\varepsilon}$ is either $\dot{\varepsilon}_{1D}$ or $\dot{\varepsilon}_{2D}$, and A and n are the rheological coefficient and exponent respectively appearing in the Schoof formula Eq. 1a. In our implementation η is computed using the velocity solution of the previous iteration (Pollard and DeConto, 2012), at the last grounded cell adjacent to the grounding line.

η does not enter in Eq. (1a), but we attempt to compensate for the absence of the 2-D strain-softening in (A3) by altering A in Eq.
(1a) by an appropriate factor:

$$A' = A \left(\frac{\dot{\varepsilon}_{2D}}{\dot{\varepsilon}_{1D}} \right)^{n-1} \tag{A4}$$

This is not rigorous because the Schoof analysis incorporates the 1-D dependence (A1) in its derivation, and not (A2). However
the modification to A in (A4) is at least in the right direction (increasing the ice flux across the grounding line), and may be
useful as a crude approximation.

A2. Overestimate of ice flux for high basal sliding coefficients

Sergienko and Wingham (2019) found that in ice streams with high basal sliding coefficients, the boundary-layer expansion of
Schoof (2007) is not valid, and can overestimate the flux of ice across the grounding zone. Following on from that paper, the
ratio of the newly calculated flux to the Schoof-calculated flux, in idealized tests for small basal slopes, ranges from ~0.6 to 1 but
can be much smaller for steeper slopes (O. Sergienko, personal communication, 2020). This analysis cannot be represented by
modifications in our model. However, we can crudely estimate the possible effect of such changes for small basal slopes at least,
by simply reducing all imposed grounding-line velocities in (1) by a constant factor, i.e., multiplying U_g given by (1b) by a factor
0.6.

A3. Effects on results

The effects of applying each of the modifications described above are shown here. Figs. A1 and A2 shows results for the
MISMIP+ Ice1 and Ice2 experiments respectively, where the effects are similar in magnitude to those shown in the main paper
(Figs. 3 and 6) due to the modifications there. By and large, the grounding-line excursions here are still within in the envelopes
of other models in the MISMIP+ intercomparison (Cornford et al, 2020).

The "sign" of the two effects in these figures is as follows: if the modification basically increases (decreases) the imposed
grounding-line flux, the rates and amplitudes of the grounding-line variations increase (decrease). The strain-softening
modification in section A1 has the former effect (increased flux, increased response), and the U_g modification in section A2 has
the latter effect (decreased flux, decreased response).
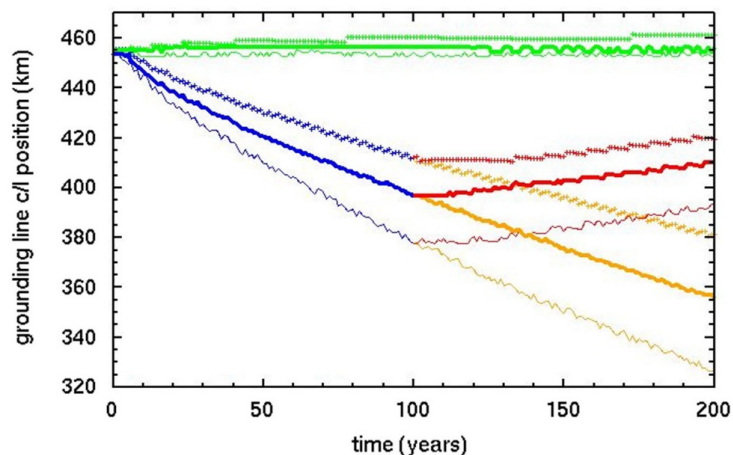
Figure A1. Along-fjord centerline position (km) of grounding lines in the MISMIP+ Ice1 experiment (Cornford et al., 2020). **Thick lines:** with new modifications in main paper (model version C). **Thin lines:** model version C and strain-softening modification in section A1. **Crosses:** model version C and U_g modification in section A2. **Green:** control (continuation of spin-up with zero oceanic melt). **Blue and yellow:** with oceanic melt perturbation. **Red:** with oceanic melt reset zero after year 100.
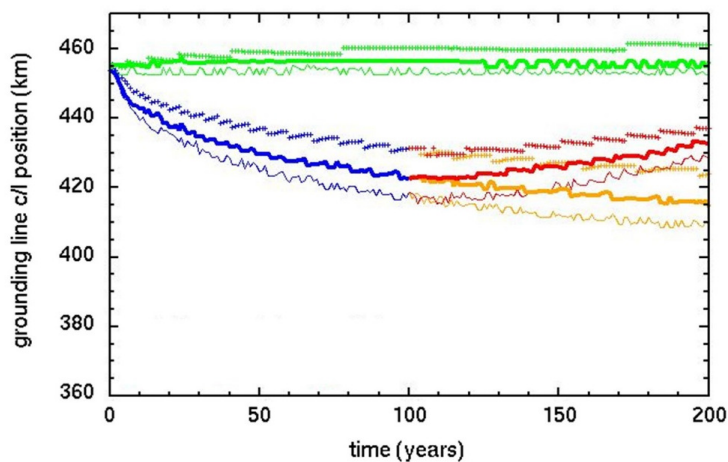
Figure A2. As Fig. A1 except for the MISMIP+ Ice2 experiment (Cornford et al, 2020).

Fig. A3 shows results for future West Antarctic retreat, for simulations without hydrofracturing or cliff failure. The modifications in the Appendix above have very little effects on equivalent sea-level rise, as also seen for the modifications in the main paper (Fig. 7); again this is presumably due to the more one-dimensional character of ice retreat in major Antarctic basins, with wider lateral scales than the narrow MISMIP+ channel.
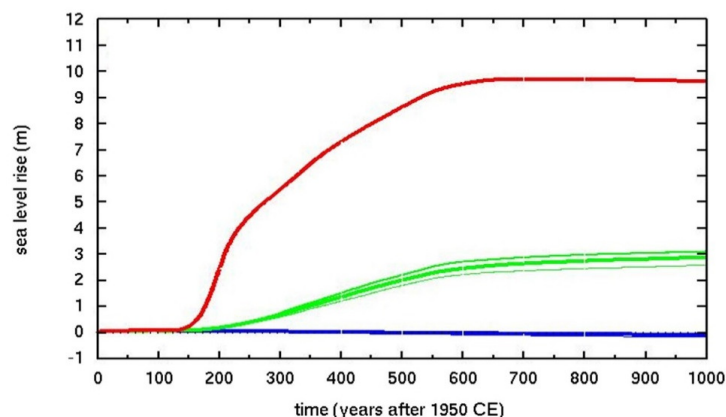
Figure A3. Equivalent global sea level rise in simulations of future West Antarctic ice retreat with climate forcing based on RCP8.5 greenhouse-gas scenario. **Thick lines:** with new modifications in main paper (model version C). **Medium lines:** model version C and strain-softening modification in section A1. **Thin lines:** model version C and U_g modification in section A2. **Blue:** control (perpetual modern climate). **Green:** with RCP8.5 forcing, without hydrofracturing or cliff failure. **Red:** with RCP8.5 forcing, with hydrofracturing and cliff failure.

430

Code and Output Availability. The ice sheet model code is available on request from the corresponding author (pollard@essc.psu.edu). That and selected model output will be available at Penn State's Data Commons, http://www.datacommons.psu.edu.

435

Author contributions. DP and RD conceived the project and design. DP performed coding and simulations and wrote the manuscript with input from RD.

Competing interests. The authors declare that they have no conflict of interest.

440

Acknowledgements. This work was supported by National Science Foundation grant NSF ICER-1663693 and National Aeronautics and Space Administration grant NASA NNH16ZDA001N-SLCST. We thank Richard Alley for helpful advice on the discussion of ice yield stress in section 5.

445 **References**

Arthern, R.J. and Williams, C.R.: The sensitivity of West Antarctica to the submarine melting feedback. Geophys. Res. Lett., 44, 252-2359, 2017.

Barletta, V.R., Bevis, M., Smith, B.E., Wilson, T., Brown, A., Bordoni, A., Willis, M., Abbas Khan, S., Rovira-Navarro, M., Dalziel, I., Smalley Jr., R., Kendrick, E., Konfal, S., Caccamise II, D.J., Aster, R.C., Nyblade, A., and Wiens, D.A.: Observed
450 rapid bedrock uplift in Amundsen Sea Embayment promotes ice-sheet stability. Science, 360, 1335-1339, 2018.

Bassis, J.N. and Walker, C.C.: Upper and lower limits on the stability of calving glaciers from the yield strength envelope of ice. Proc. Roy. Soc. A, 468, 913-931, 2012.

Bassis, J.N. and Jacobs, S.: Diverse calving patterns linked to glacier geometry. Nature Geosci., 6, 833-836, 2013.

Benn, D., Åström, J., Zwinger, T., Todd, J., and Crawford, A.: Marine ice-cliff instability: How does it work, and what controls
455 ice retreat rates? Geophysical Research Abstracts Vol. 21, EGU2019-15396, EGU General Assembly, Vienna, Austria, 2019.

Burton, J.C., Amundson, J.M., Cassotto, R., Kuo, C.-C., and Dennin, M.: Quantifying flow and stress in ice mélange, the world's largest granular material. Proc. Nat. Acad. Sci., 105, 5105-5110, 2018.

Clerc, F., Minchew, B.M., and Behn, M.D.: Marine ice cliff instability mitigated by slow removal of ice shelves. Geophys. Res. Lett., 46, 12108-12116, 2019.

460 Cornford, S.L., Seroussi, H., Asay-Davis, X.S., Gudmundsson, G.H., Arthern, R., Borstad, C., Christmann, J., dos Santos, T.D., Feldmann, J., Goldberg, D., Hoffman, M.J., Humbert, A., Kleiner, T., Leguy, G., Lipscomb, W.H., Merino, N., Durand, G., Morlighem, M., Pollard, D., Rückamp, M., Williams, C.R., and Yu, H.: Results of the third Marine Ice Sheet Model Intercomparison Project (MISMIP+), The Cryo. Disc., https://doi.org/10.5194/tc-2019-326, 2020.

DeConto, R.M. and Pollard, D.: Contribution of Antarctica to past and future sea-level rise. Nature, 531, 591-597, 2016.

465 Feldmann, J. and Levermann, A.: Collapse of the West Antarctic Ice Sheet after local destabilization of the Amundsen Basin. Proc. Nat. Acad., 112, 14191-14196, 2015.

Fretwell, P., et al.: Bedmap2: improved ice bed, surface and thickness datasets for Antarctica. The Cryosphere, 7, 375-393, 2013.

Fürst, J.J., Durand, G., Gillet-Chaulet, F., Tavard, L., Rankl, M., Braun, M., and Gagliardini, O.: The safety band of Antarctic ice shelves. Nature Clim. Change, 6, 479-482, 2016.

470 Golledge, N.R., Kowalewski, D.E., Naish, T.R., Levy, R.H., Fogwill, C.J., and Gasson, E.G.W.: The multi-millennial Antarctic commitment to future sea-level rise. Nature, 526, 421-425. 2015.

Gomez, N., Pollard, D., and Holland, D.: Sea-level feedback lowers projections of future Antarctic Ice-Sheet mass loss. Nature Commun., 6, 8798, doi:10.1038/ncomms/9798, 2015.

Gomez, N., Latychev, K., and Pollard, D.: A coupled ice sheet-sea level model incorporating 3D Earth structure: Variations in
475   Antarctica during the last deglacial retreat. J. Climate, 31, 4041-4054, 2018.

Gudmundsson, G.H.: Ice-shelf buttressing and the stability of marine ice sheets. The Cryo., 7, 647-655, 2013.

Haseloff, M. and Sergienko, O.V.: The effect of buttressing on grounding line dynamics. J. Glaciol., 64, 417-431, 2018.

Heeszel, D.S., Wiens, D.A., Anandakrishnan, S., Aster, R.C., Dalziel, I.W.D., Huerta, A.D., Nyblade, A.A., Wilson, T.J., and
Winberry, J.P.: Upper mantle structure of the central and West Antarctica from array analysis of Rayleigh wave phase velocities.
480   J. Geophys. Res. Solid Earth, 121, 1758-1775, 2016.

Jezek, K.C.: A modified theory of bottom crevasses used as a means for measuring the buttressing effect of ice shelves on inland
ice sheets. J. Geophys. Res., 89, 1925-1931, 1984.

Ma, Y., Tripathy, C.S., and Bassis, J.N.: Bounds on the calving cliff height of marine terminating glaciers. Geophys. Res. Lett.,
44, 1369-1375, 2017.

485   Nick, F.M., van der Veen, C.J., Vieli, A., and Benn, D.I.: A physically based calving model applied to marine outlet glaciers and
implications for the glacier dynamics. J. Glaciol., 56, 781-794, 2010.

Nye, J.F.: The distribution of stress and velocity in glaciers and ice sheets. Proc. Roy. Soc. A, 239, 113-133, 1957.

Parizek, B.R, Christianson, K., Alley, R.B., Voytenko, D., Vaňková, I., Dixon, T.H., Walker, R.T., and Holland, D.M.: Ice-cliff
failure via retrogressive slumping. Geology, 47, 449-452, 2019.

490   Pollard, D. and DeConto, R.M.: Description of a hybrid ice sheet-shelf model, and application to Antarctica. Geosci. Model
Devel., 5, 1273-1295, 2012.

Pollard, D., DeConto, R.M., and Alley, R.B.: Potential Antarctic Ice Sheet retreat driven by hydrofracturing and ice cliff failure.
Earth Plan. Sci. Lett., 412, 112-121, 2015.

Pollard, D., DeConto, R.M., and Alley, R.B.: A continuum model (PSUMEL1) of ice mélange and its role during retreat of the
495   Antarctic Ice Sheet. Geosci. Model Devel., 11, 5149-5172, 2018.

Powell, E., Gomez, N., Hay, C., Latychev, K., and Mitrovica, J.X.: Viscous effects in the solid Earth response to modern
Antarctic ice mass flux: Implications for geodetic studies of WAIS stability in a warming world. J. Clim., 33, 443-459, 2020.

Reese, R., Winkelmann, R. and Gudmundsson, H.: Grounding-line flux formula applied as a flux condition in numerical
simulations fails for buttressed Antarctic ice streams. The Cryosphere, 12, 3229-3242, 2018.

500   Schlemm, T. and Levermann, A.: A simple stress-based cliff-calving law. The Cryo., 13, 2475-2488, 2019.

Schoof, C.: Ice sheet grounding line dynamics: steady states, stability, and hysteresis. J. Geophys. Res. - Earth Surf., 112,
F03S28, doi: 10.1029/2006JF000664, 2007.

Sergienko, O.V. and Wingham, D.J.: Grounding line stability in a regime of low driving and basal stresses. J. Glaciol., 65, 833-849, 2019.

505 Shields, C.A., Kiehl, J.T., and Meehl, G.A.: Future changes in regional precipitation simulated by a half-degree coupled climate model: Sensitivity to horizontal resolution. J. Adv. Model. Earth Syst., 8, 863-884, 2016.

Thoma, M., Grosfeld, K., Barbi, D., Determann, J., Goeller, S., Mayer, C., and Pattyn, F., RIMBAY – a multi-approximation 3D ice-dynamics model for comprehensive applications: model description and examples. Geosci. Model Dev., 7, 1-21, 2014.

Turcotte, D.L. and Schubert, G.: Geodynamics Applications of Continuum Physics to Geological Problems. J. Wiley Publ., 450
510 pp, 1982.